Low Temperature Plasma Technology Laboratory

Large-area helicon plasma source with permanent magnets

Francis F. Chen and Humberto Torreblanca

LTP-605   May, 2006

Electrical Engineering Department
Los Angeles, California 90095-1594

UNIVERSITY OF CALIFORNIA • LOS ANGELES

Large-area helicon plasma source with permanent magnets

Francis F. Chen and Humberto Torreblanca

Electrical Engineering Department, University of California, Los Angeles, CA 90095-1594

ABSTRACT

A helicon plasma source has been designed using annular permanent magnets to produce the required DC magnetic field (B-field). With the discharge tube located in the remote field, rather than the internal field of the magnet rings, the plasma can be injected into a processing chamber containing the substrate to be treated. The discharge tube, radiofrequency (RF) antenna, and magnet size were optimized by computation and tested by experiment. A distributed source comprising eight individual discharges was constructed and tested. Such sources are capable of producing downstream densities $> 10^{12}$ cm^{-3} (in argon) over an arbitrarily large area for high-flux applications.

I. INTRODUCTION

Unlike other RF plasma sources, helicon sources depend on the excitation of waves, namely, helicon waves, which are whistler waves bounded within a cylinder. The behavior of these waves and of the discharges they produce has provided numerous challenges to our intuition. Foremost among these is the efficient ionization mechanism which causes the density to be as much as an order of magnitude higher than that in other plasma generators at a given power. In 1991 Chen[1] suggested that ionizing electrons were accelerated by Landau damping. Though a small number of such electrons has been detected, the Landau damping hypothesis was later disproved by Chen and Blackwell[2], who showed that these electrons were too few to produce the high observed densities. Meanwhile Shamrai and Taranov[3] proposed that electron cyclotron waves in the Trivelpiece-Gould (TG) mode could be generated by mode-coupling at the radial boundary. These electrostatic modes rapidly convert RF energy into electron heat. The existence of TG modes was confirmed in the experiment of Blackwell et al.[4], and computations[5] support the dominance of this mechanism in the far-field region downstream from the antenna. Near the antenna the fields are so strong that they cannot be measured easily. Nonlinear or parametric coupling to ion acoustic or lower-hybrid waves have been suggested. Using correlation techniques, Lorenz et al.[6] proved the existence of parametric decay of helicons into ion acoustic and TG modes. Energy deposition in helicon discharges is, therefore, very complicated, but it works.

At least two companies have tried to commercialize helicon sources for plasma processing. The device of Chapman et al.[7] employed a Boswell[8] antenna to create an $m = 1$ helicon wave, where m is the azimuthal wave number. The device of Campbell et al.[9], described by Tynan et al.[10], used a dual $m = 0$ antenna with opposite currents. Though both sources performed well, they were not readily accepted by the semiconductor industry, which found that simpler RF sources not requiring DC B-fields were satisfactory for substrates up to 300-400 mm in diameter.

For applications to larger substrates, the idea of distributed sources using multiple discharges has been tried with both magnetic and field-free systems. In particular, Chen et al.[11] made extensive measurements of a seven-tube helicon source, proving the principle that uniform plasmas can be produced with a finite number of discrete sources. However, the magnetic field

was still a problem. If the field was produced by a small coil around each tube, the field lines diverged so rapidly that most of the plasma was carried into the entrance flange and lost there before reaching the processing chamber[12]. To avoid this, a uniform B-field was produced with a large electromagnet surrounding the entire array. Also, the discharge tube and the antenna were shortened to reduce the wall loss. This device[11] produced a plasma of nearly 10^{12} cm^{-3} density, uniform to 3% over 400 mm. Similar results have been reported by Kim et al.[13] in a 12-tube linear array. However, this concept cannot be extended to much larger areas; and the large, expensive magnet and its power supply make the device uneconomical for commercial purposes. The use of permanent magnets (PMs) alleviates this problem

II. CHARACTERISTICS OF TOROIDAL PMs

Consider a stack of ring magnets magnetized vertically, as shown in Fig. 1. A uniform downward B-field exists inside the hole of the stack, and strong helicon discharges can be produced there. However, the plasma cannot escape from the hole, since those field lines end on the magnets. At large distances, the hole is insignificant, and the stack appears as a simple dipole, with the field pointing upwards. Thus, there must be a stagnation point on axis where the field reverses sign. If the plasma is created in the external field beyond the null, the field is weaker and not as uniform, but it extends to infinity. In practice, the null point occurs very close to the magnets, and a compact system can still be designed.
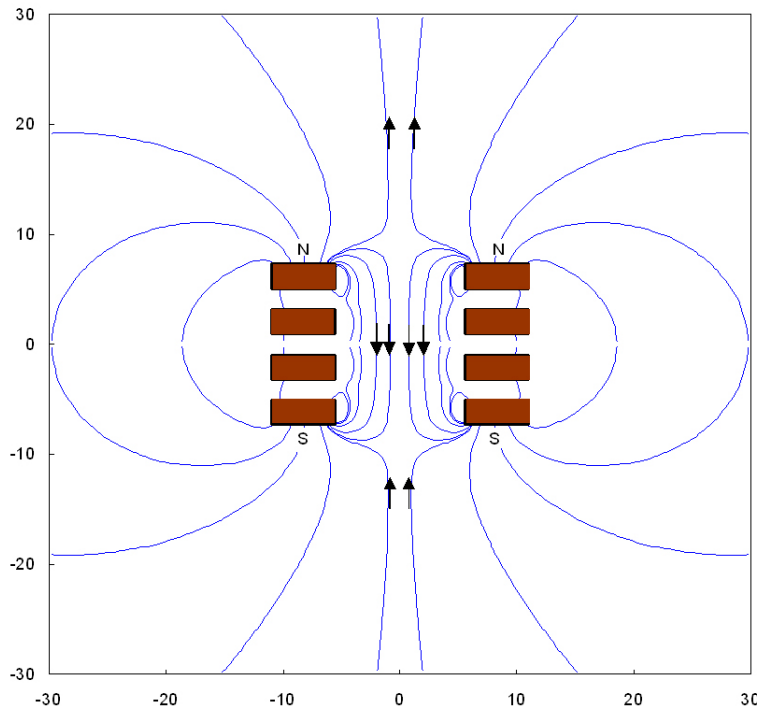

Fig. 1. Field lines around a stack of annular ceramic magnets 2.2 cm thick and 1.9 cm apart.

Figure 2 shows the computed and measured B-fields on axis, showing the field reversal at $z \sim 10$ cm below the midplane of the stack. The reverse-field, remote region is shown in Fig. 3, together with different test positions of the discharge tube, showing the field gradients. These positions sampled B-fields of ~100G down to below 20G. Calculations were made to optimize the shape of the magnets as their inner and outer diameters (ID, OD) and their thickness and spacing were varied. The results showed that field strength increased more or less with the total volume of the magnets and decreased with the spacing. Uniformity of the remote field improved with spacing, and hence the configuration of Fig. 1 was chosen for our tests.
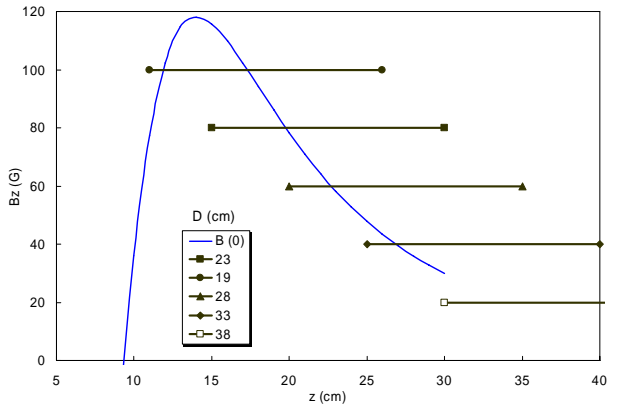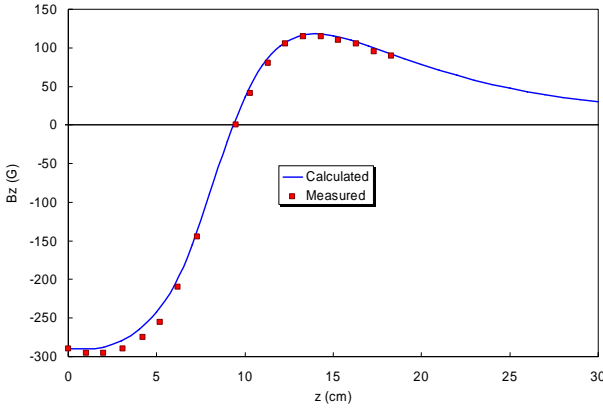
2

Fig. 2 (left). Computed $B_z(z)$ on axis compared with measurements, where z is measured from the midplane of the magnet stack.

Fig. 3 (right). $B_z(z)$ in the remote region. The lines represent the length of the discharge tube as it is placed at various distances below the magnets. Here D is the distance between the bottom of the magnet stack and the bottom of the discharge tube.

III. PRELIMINARY TESTS IN THE REMOTE FIELD

Tests with these magnets were made with the apparatus shown in Fig. 4. The discharge tube was a 7.6-cm ID Pyrex pipe 15.2 cm long. Up to 500 W of RF at 2 or 13.56 MHz was applied to an $m = 0$ loop antenna at the midplane of the tube. The gas was $1-10$ mTorr of argon. Density profiles were measured with two Langmuir probes located at $Z1 = 7.4$ cm and $Z2 = 17.6$ cm below the top flange.

Radial density profiles $n(r)$ for various heights D are shown in Fig. 5 for 2 MHz, 1 mTorr, and 500W. The low density at $D = 1$ cm proved that putting the discharge inside the magnets produces low n downstream, though that inside the tube was high. Though the densities were much higher than with $\mathbf{B} = 0$, they were only in the mid-10^{10} cm^{-3} range, rather than the high 10^{11} cm^{-3} range, as obtained previously[11]. The density increased with increasing D, where $\mathbf{B}$ was weakest. This was probably caused by the difference in field line divergence, which also could have caused the large change in profile between Z1 and Z2. Increasing the pressure to 10 mTorr had little effect.
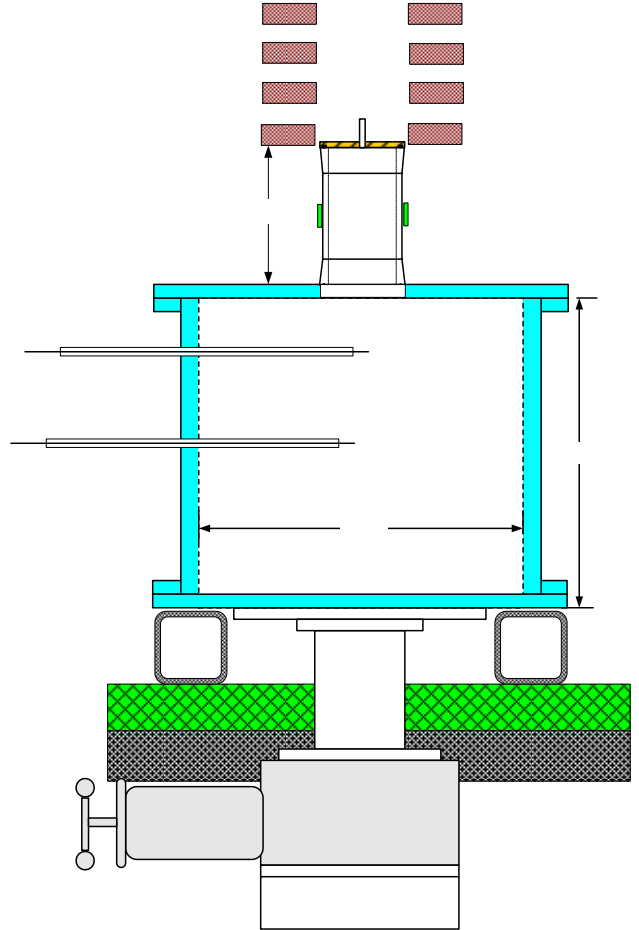

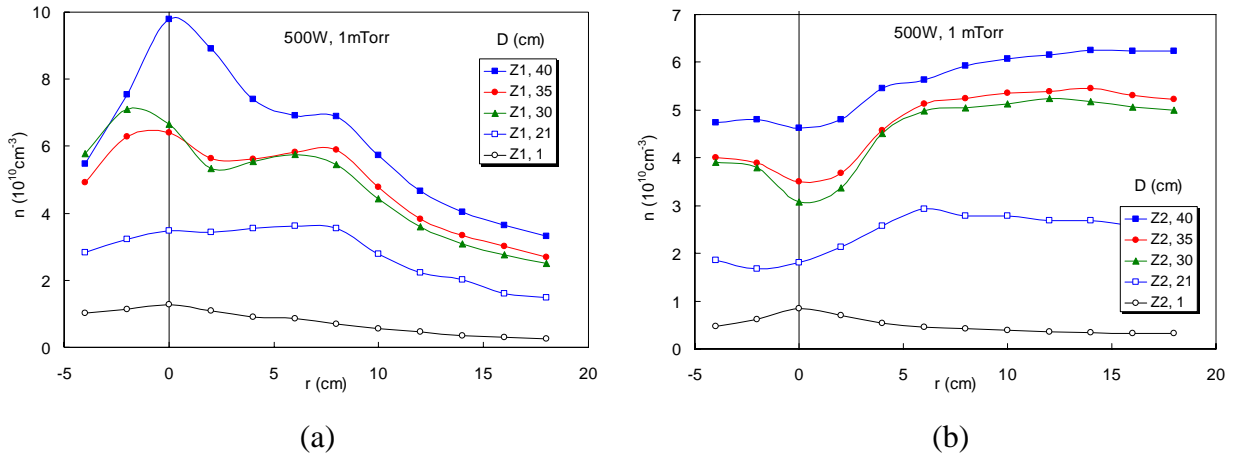Fig. 4. Schematic of apparatus for first tests of helicon discharges in the remote field.

3

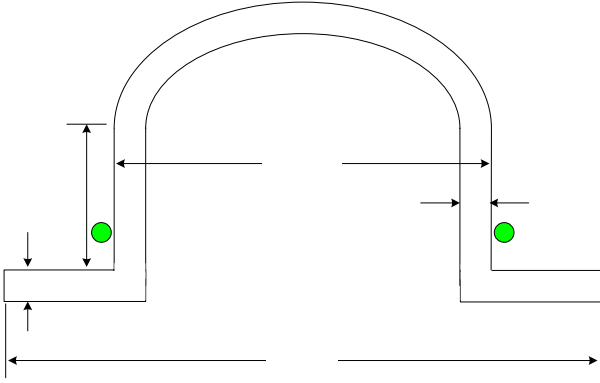Fig. 5. Radial density profiles at Z1 and Z2 for various magnet positions D. Conditions: 500W at 2 MHz, 1 mTorr.
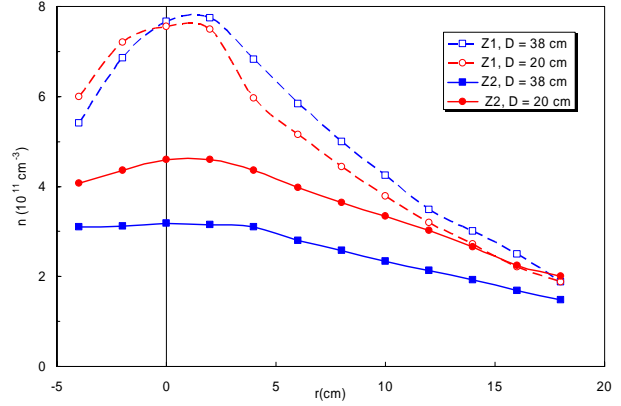

Fig. 6 (left). Diagram of the short "stubby" tube.

Fig. 7 (right). Density profiles with the "stubby" tube at 500W and 10 mTorr. Dashed (- - -) curves are for probe position Z1, and solid (——) curves for Z2. Squares (□) are for D = 38 cm, and circles (○) for D = 20 cm.

To recover previous results, we replaced the 7.6-cm diameter tube with the short, 5-cm-diam tube used in Ref. 11 and shown in Fig. 6. As seen in Fig. 7, $n(r)$ increased by an order of magnitude, and the behavior with radius and pressure was more reasonable. This is because the antenna created plasma close to the exit aperture, with little loss to the sidewalls in spite of the diverging B-field. Furthermore, the added flat section moved the plasma farther from the metal flange, minimizing image currents and electron losses. The insulating corner also mitigates these losses by charging to a negative floating potential. A small $m = 0$ antenna is essential. Helical or Nagoya Type III $m = 1$ antennas require long tubes and create plasma far from the exit hole. Experiments with other antennas yielded poor results downstream.

IV. OPTIMIZATION

1. The low-field peak and plasma loading. To optimize the discharge tube, numerous computations were made with the HELIC code of D. Arnush[14]. This code yields the plasma resistance R of a coupled helicon-TG wave in an infinite or finite-length cylinder for specified B, $n(r)$, pressure, and antenna type. However, **B** and n are assumed uniform in the axial (z) direction. To simulate injection from a short tube into a large space, a 2-m long cylinder is assumed, and the antenna is placed a small, set distance from one endplate. A typical $n(r)$ profile is assumed.

4

Since B in the far-field region of a PM is likely to be weak, we take advantage of the density peak found at low B in helicon discharges[15]. This has been explained by constructive reflection from the endplate[16]. The location of this peak depends on the density, plasma radius, and endplate conductivity. Since B is fixed while n varies in an experiment, it is convenient to show the peak as a function of n rather than of B. An example of R vs. n is shown in Fig. 8. The density at the peak varies linearly with B, as in simple helicon theory.
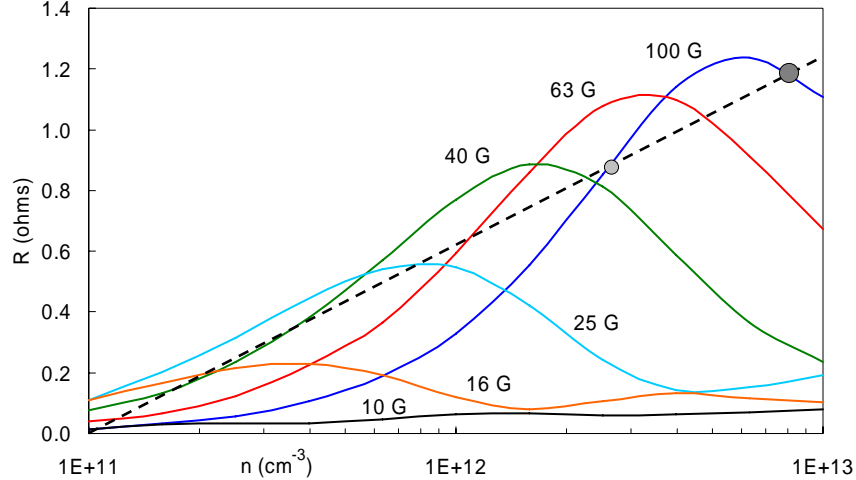

Fig. 8. Plasma resistance vs. density at various B-fields at 1 mTorr for a 5-cm diam tube, 5 cm long, with a conducting endplate. The dashed line represents losses proportional to n, intersecting the 100-G curve at two points, the leftmost one being unstable.

The value of R is related to the RF power absorption P_{in}, and hence to n, as follows. If P_{rf} is the power out of the generator and R_c is the circuit resistance, P_{in} is given by

$$P_{in} = P_{rf}\frac{R_p}{R_p + R_c}. \tag{1}$$

If $R_p \ll R_c$, $P_{in} \propto R_p$, and both stable and unstable intersections with the loss curve can occur[17]. We desire $R_p \gg R_c$, so that $P_{in} \approx P_{rf}$. Power balance determines n. Consider a discharge 5 cm in diam and 5 cm long, with surface area S ~ 122 cm^2. At low pressure the ion flux to the walls is $\Gamma_i \approx \frac{1}{2}nc_s$, where the acoustic velocity c_s is 1.7×10^5 cm/sec at $KT_e = 3$ eV in argon. The particle loss rate is then

$$-dN/dt = \frac{1}{2}Snc_s = 1.0 \times 10^7 n \quad \text{sec}^{-1}. \tag{2}$$

The energy loss is the sum of three terms[18,19]:

$$W = E_c + W_i + W_e, \tag{3}$$

where W_i and W_e are the ion and electron energies carried out, and E_c is the energy lost to radiation in each ionization, as computed by Vahedi[20]. Each escaping ion loses its energy gained in the presheath ($\frac{1}{2}KT_e$) and that gained in the wall sheath (~$5KT_e$), a total of W_i ~ $5.5KT_e$. The accompanying electron loses $2KT_e$[18,19]. Eqs. (2) and (3) then yield

$$P_{out} \approx 1.1 \times 10^{-10} n \text{ Watts}. \tag{4}$$

This line is shown in Fig. 9 together with P_{in} computed from Eq. (1) and the 100-G curve of Fig. 8, assuming $R_c = 0.1\Omega$. We see that P_{in} is close to P_{rf}, and unstable intersections have been eliminated as long as R_p / R_c is greater than about 10.
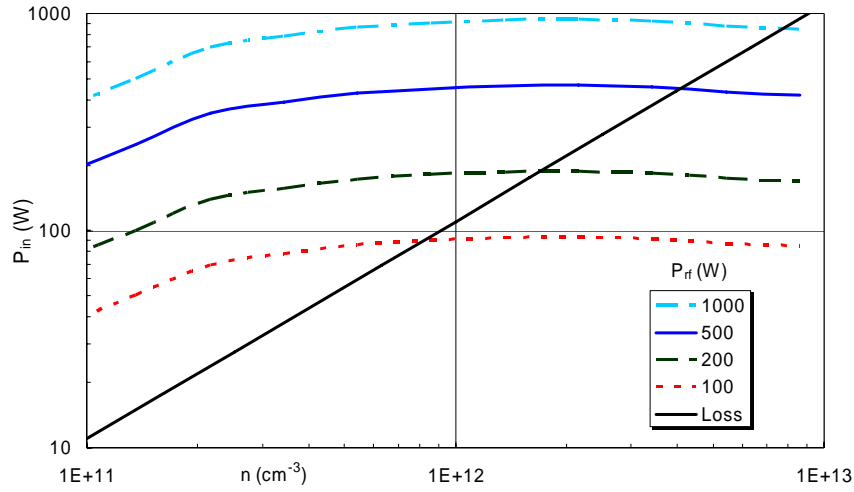
5

Fig. 9. Absorbed power for various applied powers vs. density. The diagonal line is the computed energy loss rate.

2. Tube design. HELIC calculations of loading resistance vs. tube diameter *d* are shown in Fig. 10. It appears that larger diameters are better, but this is illusory. First, the large *R* can be achieved only by increasing the power more than the volume ratio. More importantly, the larger antenna has such a high inductance even for a single turn that very large capacitors are required in the matching circuit. With small *d*, the inductance can be varied to suit the matching network by varying the number of turns in the *m* = 0 antenna. Experiments with a 15-cm diam tube at 500W produced only a faint glow under the antenna, with densities at Z1 in the mid-10^{10} cm^{-3} range. Similarly, computations varying the distance between the antenna and the endplate were deceptive. Density was always higher when the antenna is placed near the exit aperture.
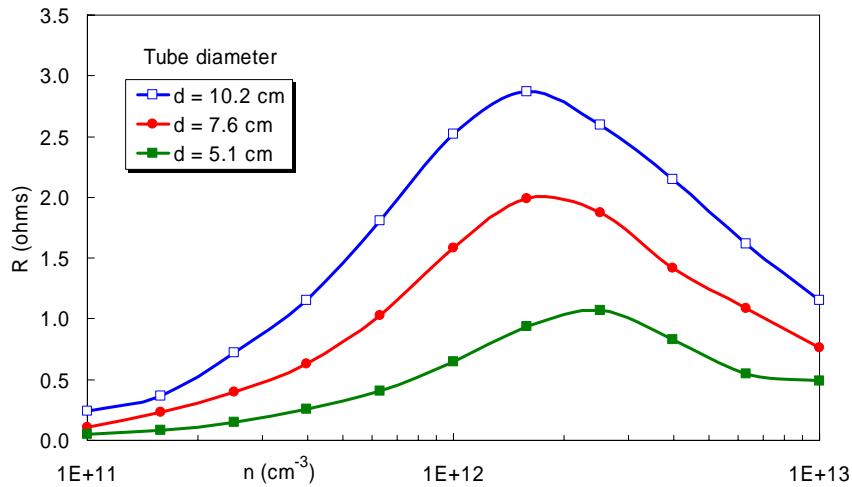

Fig. 10. *R* vs. peak density *n* for various diameters *d* at 13.56 MHz and 3 mTorr. The antenna is a simple loop located 5 cm from a conducting endplate. Parabolic *n(r)* profile; KT_e = 2.5 eV.

Frequency dependence is shown in Fig. 11. For the range of *n* and *B* being considered, the higher frequency gives much larger loading. The harmonic at 27.12 MHz is advantageous only at much higher *B* and *n*. Figure 12 shows the effect of endplate material. Conducting endplates are generally better for our range of parameters. As a result of these studies, the tube design of Fig. 13 was adopted. It is very similar to the intuitive design of Fig. 6.
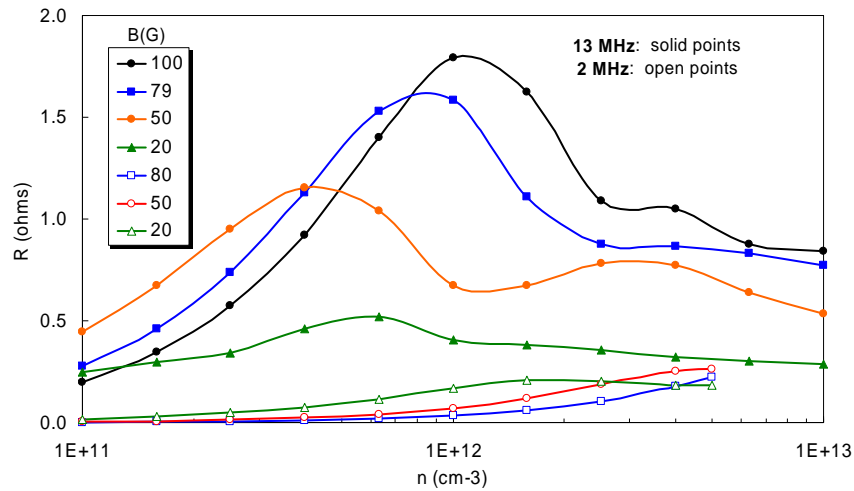
Fig. 11. *R* vs. *n* at various B-fields for a 7.6 cm diam tube at 2 and 13.56 MHz.
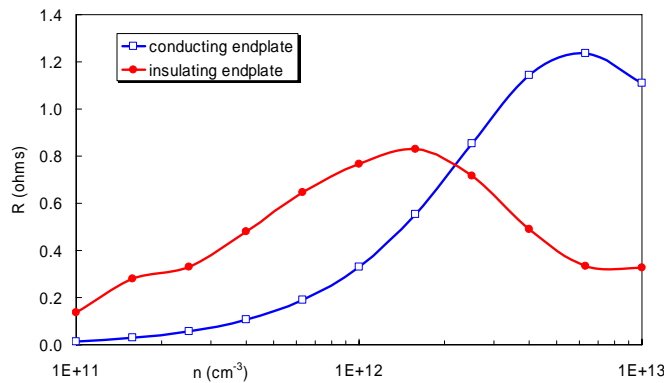

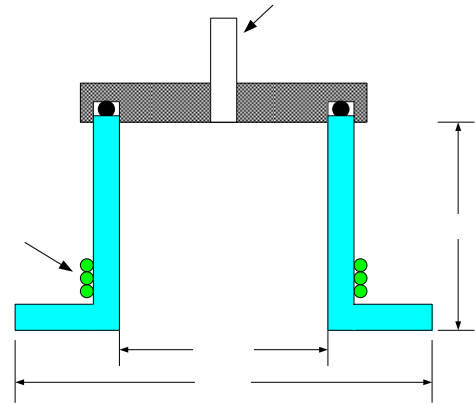Fig. 12 (left). Comparison of endplates for a 5-cm diam tube at 100G.

Fig. 13 (right). Optimized design of discharge tube.

3. Magnet design

Permanent magnets can be made of ceramic, Alnico, SmCo, or NdFeB (the strongest). Ceramic magnets are cheapest, but when tooling cost is included, Nd magnets are actually cheaper. These have an internal field of 12 kG and therefore need not be thick. They can also be small to go with the 5-cm diam tubes. We therefore decided on Nd magnets of 7.6 cm ID and 12.7 cm OD, 2.54 cm thick. Their field lines are shown in Fig. 14, together with positions of the discharge tube to adjust field strength and uniformity. Figure 15 plots *B* vs. *r* at various distances *z* below the magnet. At the

Fig. 14. Field pattern of Nd magnets. The rectangles below them represent possible positions of the discharge tube.

7
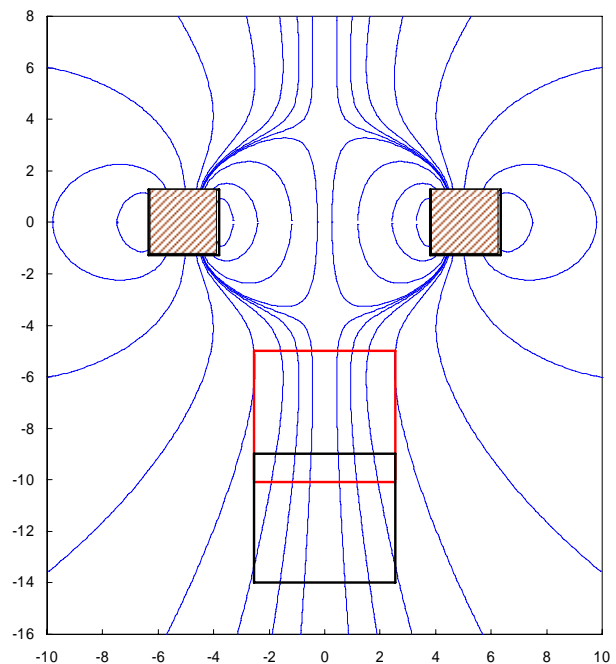
indicated position of the tube, the field is very uniform radially but varies from 175 to 75G from top to bottom. The magnets are so strong that one can jump 30 cm upwards to attach to another. At a separation of 1 cm, the attractive force is of order 50 kg weight.
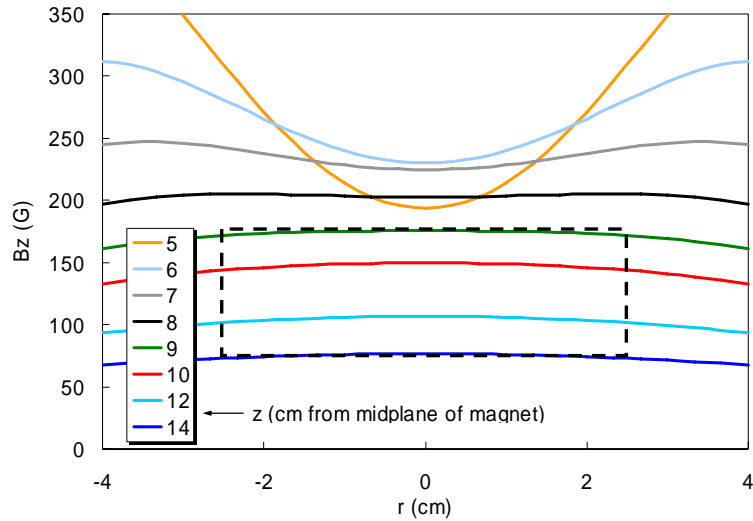

Fig. 15. B_z vs r at various z below the midplane of the magnet. The curves are in the same order as the in the legend. The dashed rectangle is possible position of a 5-cm diam $\times$ 5 cm long discharge

V. AN ARRAY OF OPTIMIZED SOURCES

The spacing between tubes was determined by superposing $n(r)$'s from neighboring tubes to obtain the total density. The $n(r)$ from a single tube and its magnet is shown in Fig. 16. The disturbance from neighboring magnets is minimal. A test facility was built with flexible source deployment, as shown in Fig. 17. For application to web-coaters, the staggered array is used. For more uniformity and higher density, the outermost tubes can be moved into the positions shown in lighter color to form a more compact array. The density at substrate level, Z2 = 17.6 cm below the tubes, is calculated from a fit to the lower curves in Fig. 16. The ripple between tubes in one row is shown in Fig. 18 *vs*. the distance L between tubes. It is seen that $L = 17.5$ cm gives a ripple of ±2%; hence the spacing chosen in Fig. 17.
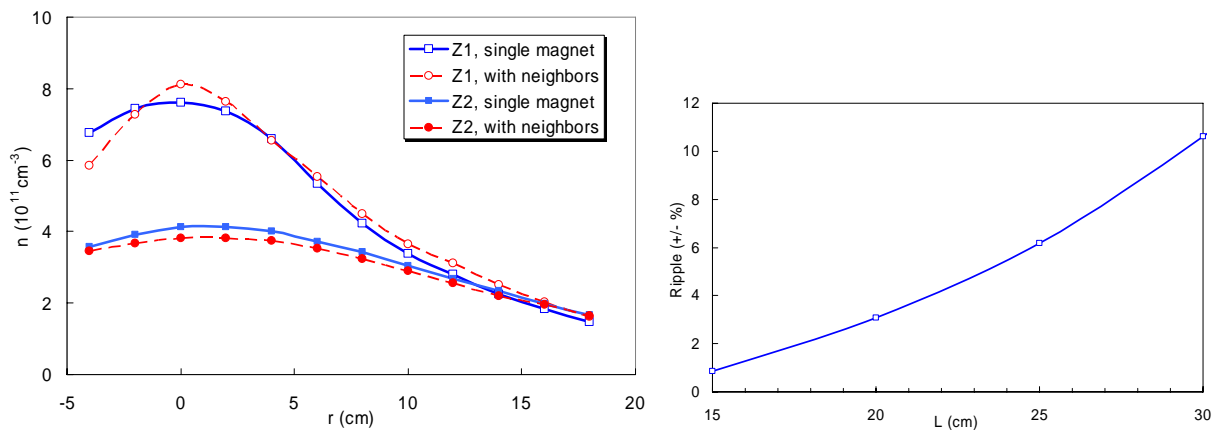

Fig. 16 (left).   Density profiles (——) for a single tube and magnet at probe positions Z1 and Z2. The dashed curves (- - -) are for a single tube in the presence of the other magnets. (500W, 15 mTorr).

Fig. 18 (right). Computed ripple between tubes at Z2 vs. tube separation L.
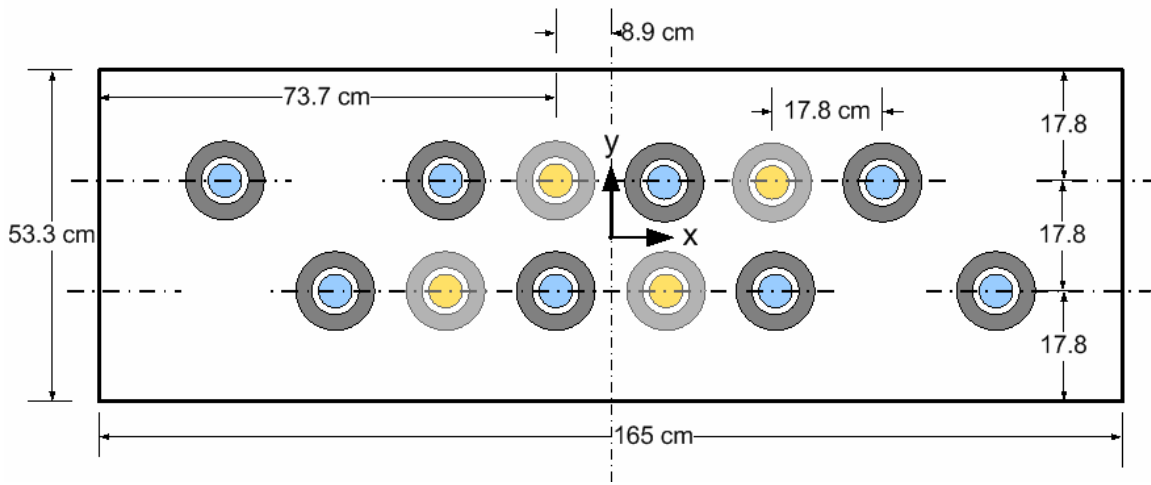
8

Fig. 17. Spacing of sources in an 8-tube array.

For the two-row staggered configuration, the density $n(x)$ is computed for the four central tubes at various y (Fig. 19). At $y = 0$ the ripple is very small, each row contributing equally to n. At $y = 15$, directly beneath one row, the ripple is large, and the other row contributes little. In a web-coater, as the substrate moving in the y direction passes under both rows, it experiences an average density shown by the thick line in all views.
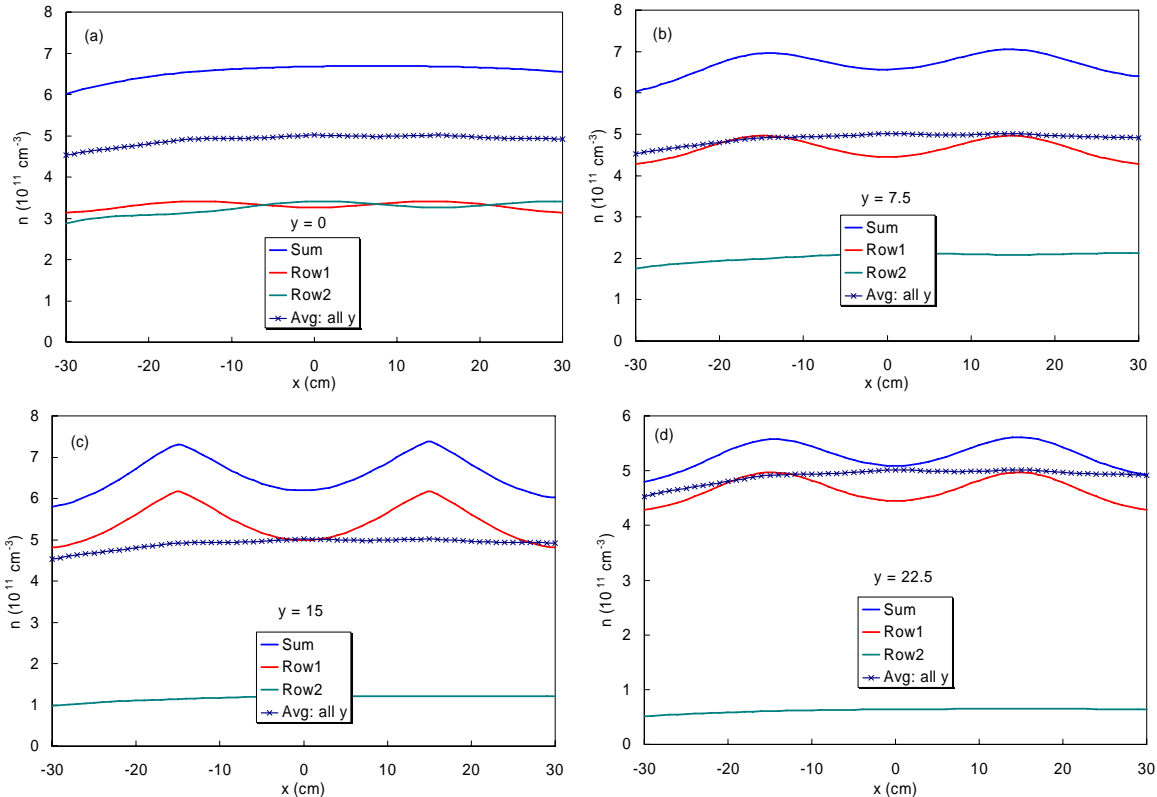

Fig. 19. Density distribution $n(x)$ at $y = 0$, 7.5, 15, and 22.5 cm for two staggered rows, 30 cm apart, each comprising two tubes separated by 30 cm. The bottom curves give the contribution from each row separately, and the top curve is the sum. The thick line, the same in (a)–(e), is the density averaged over all y. The roll-off at large x would not exist for a full row of tubes.

A side view of the setup in Fig. 20 shows two of the tubes and magnets and four diagnostic ports. The magnets are adhered to a ferromagnetic plate which can be moved

9

vertically to vary the spacing and thus the field strength. However, once stuck to the iron, the magnets are very hard to move. For adjustments in testing, the magnets are placed in wooden partitions, shown in Fig. 21, which also serve as safe storage. The magnets are held in place by dowels. When placed in the same plane with the same polarity, the magnets repel and do not tend to flip onto each other in a dangerous manner.
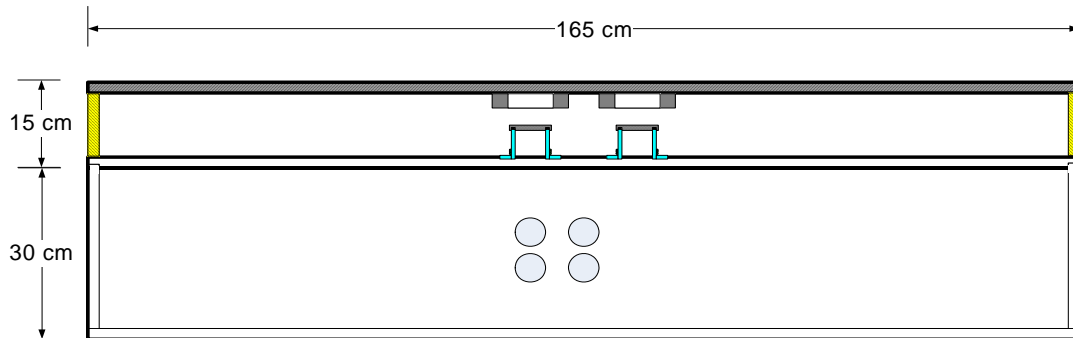

Fig. 20. Side view of test device.

Fig. 21   Magnet storage and positioning frame.

An eight-tube array operating in the helicon mode is shown in Fig. 22. The eight antennas are connected in parallel to a single match circuit and 3-kW RF supply with cables of equal length. Density measurements are in progress at the time of this conference.

VI.   CONCLUSION

The use of the remote field of annular permanent magnets enables uniform coverage of large substrates with high-density plasma in a vertically compact source. This device[21] can be used in web-coaters, for etching of flat panel displays, and for deposition of optical coatings. This work was supported by the National Science Foundation, Grant No. DMI-0115570.
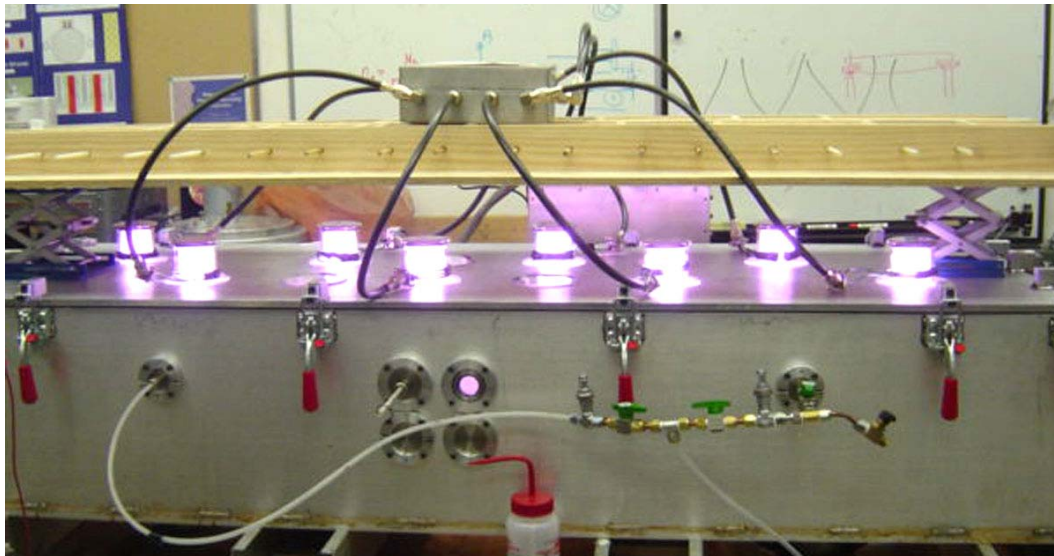
Fig. 22. The test source in staggered configuration in operation.

REFERENCES

[1] F.F. Chen, Plasma Phys. Control. Fusion **33**, 339 (1991).

[2] F.F. Chen and D.D. Blackwell, Phys. Rev. Lett. **82**, 2677 (1999).

[3] K.P. Shamrai and V.B. Taranov, Plasma Sources Sci. Technol. **5**, 474 (1996).

[4] D.D. Blackwell, T.G. Madziwa, D. Arnush, and F.F. Chen, Phys. Rev. Lett. **88**, 145002 (2002).

[5] D. Arnush, Phys. Plasmas **7**, 3042 (2000).

[6] B. Lorenz, M. Krämer, V.L. Selenin, and Yu.M. Aliev, Plasma Sources Sci.Technol. **14,** 623 (2005).

[7] B. Chapman, N. Benjamin, C.F.A. van Os, R.W. Boswell, and A.J. Perry, 12th Symposium on Dry Process, Denki-Gakkai, Tokyo (1991).

[8] R.W. Boswell, Plasma Phys. Control. Fusion **26**, 1147 (1984).

[9] G.A. Campbell, D.I.C. Pearson, and A.P. deChambrier, Proc. 33rd Annual Techn. Conf., Society of Vacuum Coaters (1990).

[10] G.R. Tynan, A.D. Bailey III, G.A. Campbell, R. Charatan, A. de Chambrier, G. Gibson, D.J. Hemker, K. Jones, A. Kuthi, C. Lee, T. Shoji, and M. Wilcoxson, J. Vac. Sci. Technol. A **15**, 2885 (1997).

[11] F.F. Chen, J.D. Evans, and G.R. Tynan, Plasma Sources Sci. Technol. **10**, 236 (2001).

[12] F.F. Chen, X. Jiang, and J.D. Evans, J. Vac. Sci. Technol. **A 8**, 2108 (2000).

[13] Y.J. Kim, S.H. Han, W. Hwang, and Y.S. Hwang, Thin Solid Films **435**, 270 (2003).

[14] D. Arnush, Phys. Plasmas **7**, 3042 (2000).

[15] F.F. Chen, X. Jiang, J.D. Evans, G. Tynan, and D. Arnush, Plasma Phys. Control. Fusion **39**, A411 (1997).

[16] F.F. Chen, Phys. Plasmas **10**, 2586 (2003).

[17] K.P. Shamrai, Plasma Sources Sci. Technol. **7**, 499 (1998).

[18] M.A. Lieberman and A. J. Lichtenberg, *Principles of Plasma Discharges and Materials Processing* (Wiley, New York, (1994), 2nd ed., p. 333.

[19] F.F. Chen and J.P. Chang, *Principles of Plasma Processing* (Kluwer/Plenum, New York, 2002), p. 71.

[20] V. Vahedi, *Thesis*, University of California, Berkeley (1993).

[21] Patent pending.